ORIGINAL PAPER

A simple route to constructing rGO wrapped Fe_2O_3 cubes as a high-performance anode material for lithium-ion batteries

Ju Zhou[1] · Xiaojuan Yang[1] · Jitong Wang[1,2] · Cheng Ma[1,2] · Wenming Qiao[1,2] · Licheng Ling[1,2]

Abstract

Combining iron oxide with carbon materials such as graphene oxide is an effective measure to solve the issues of terrible electronic conductivity and serious volume effect of iron oxides. Fe_2O_3/reduced graphene oxide nanocomposite was synthesized via simple hydrothermal method with cubic iron oxide of a uniform particle size distribution (~50 nm), which were encapsulated between reduced graphene oxide layers. Construction of nanostructure cubic iron oxide facilitates the transportation of lithium ions and electrons. Furthermore, the introduction of reduced graphene oxide promotes the conductivity and structural integrity of the nanocomposites, while avoids the agglomeration and crushing of iron oxide particles during the lithiation/de-lithiation, facilitating the storage of lithium ions. Fe_2O_3-rGO-c0.2 as an anode material exhibits superior electrochemical performance, with initial discharge capacity of 1580.6 mAh g^{-1} and reversible capacity of 1145.4 mAh g^{-1} after 100 cycles at the current density of 200 mA g^{-1}. Moreover, it has a good rate performance of 479.1 mAh g^{-1} at a current density of 5000 mA g^{-1}.

Introduction

With the rapid improvement of electric vehicles and portable electronics and the extent of power grids, the demands for energy storage equipment are getting higher [1], because of the high energy density, good safety, suitable working voltage [2], and long service life that lithium-ion batteries (LIB) have got wide attention [3]. At present, a period of time has passed since the commercialization of LIB; however, it still adopts graphite (theoretical capacity is 372 mAh g^{-1}) as the anode [4], which can no longer satisfy the requirements of the current development environment for LIB [5]. Therefore, the development of LIB anode materials with high energy density, good cycling stability, and high safety is imminent [6, 7]. Transition metal oxides, such as iron oxides [8], cobalt oxides [9], and nickel oxides [10], are able to achieve the excellent energy density and power density of LIBs which have attracted much attention as electrode materials [11].

Fe_2O_3 has been researched in depth owing to the higher theoretical capacity (1007 mAh g^{-1}) [12], abundant natural content, easy preparation, low cost, and environmentally friendly [7, 13, 14]. However, when adopted it as the anode material for LIBs, Fe_2O_3 has the following disadvantages: (1) poor electronic/ion conductivity. Poor conductivity in the transport channel is not conducive to the rapid insertion/extraction of Li^+ [15]. (2) The volume will change greatly during charging and discharging [16]. The volume will expand/shrink during the cycling, leading to agglomeration or crushing of Fe_2O_3 particles [17], which in turn bring about rapid capacity decay or terrible cycle performance and rate performance [18]. Due to these drawbacks, the practical application of iron oxide in negative electrode materials is

✉ Jitong Wang
  wangjt@ecust.edu.cn

✉ Wenming Qiao
  qiaowm@ecust.edu.cn

1   State Key Laboratory of Chemical Engineering, East China University of Science and Technology, Shanghai 200237, China

2   Key Laboratory of Specially Functional Polymeric Materials and Related Technology, East China University of Science and Technology, Shanghai 200237, China

severely restricted [19]. Current research has concluded several useful approaches that have been found to enhance the capability of transition metal oxides used as anode materials for LIBs: (1) construction of nanostructure materials. The construction of a variety of iron oxide nanoscales such as nanoparticles, nanorods, and nanosheets effectively restrains the self-aggregation of iron oxides, providing a higher specific surface area to expose more active sites and effectively shorten the lithium-ion diffusion path [19, 20]. (2) Choosing the suitable coating material and using the characteristics of the coating layer to enhance the electrochemical properties of the electrode materials [21, 22]. Moreover, other heteroatoms can be doped in the coating layer, which can also supply extra active sites to store lithium ions on the basis of improving the conductivity of the metal oxide electrode [23, 24]. (3) Combination with other materials, by the conductivity and mechanical stability of the introducing material, the volume expansion effect of the iron oxide particles is alleviated, and the problem of powdering of the electrode is further solved [25].

Combination of metal oxides with carbon materials is one of the most effective methods to enhance conductivity and structural stability of electrodes, and this strategy can endow materials with high-rate performance and cycling stability [7, 26]. Carbon materials have good mechanical flexibility and can effectively accommodate the volume changes of metal oxides [27]. In addition, good electrical conductivity and excellent specific surface area are beneficial to the diffusion and transportation of Li^+ [28], and accelerate the wettability of electrolyte and active materials [29]. Two-dimensional GO has the larger specific surface area (~ 2600 m^2 g^{-1}) [30] and excellent conductivity and structural stability; therefore, it is an expected electrode material for achieving outstanding capacity of LIBs [31, 32]. However, when it is used as electrode materials alone, graphene will re-stack, making the performance far lower than the theoretical value [33]. At present, many studies have proven that combining Fe_2O_3 and GO to prepare nanocomposites with a certain mesoporous structure can achieve a good enhancement in the performance of LIBs [34]. Cao et al. [35] synthesize the Fe_2O_3 hollow sphere/carbon nanotube (Fe_2O_3/CNT) composites by hydrothermal reaction. Due to the increase in conductivity and the effective relief of volume expansion, the composite demonstrated excellent reversible capacity of 1176.1 mAh g^{-1} at 100 mA g^{-1}. Chen et al. [36] fabricate the γ-Fe_2O_3/porous carbon fibers (γ-Fe_2O_3/PCF), the particles distributed in the CFs homogenously, which promotes the electronic conductivity and accelerates the wettability of electrolyte. Moreover, γ-Fe_2O_3/PCF delivered outstanding capability of 980 mAh g^{-1} at 0.1 C in LIB.

Herein, a simple one-step hydrothermal scheme was adopted to synthesize the cubic iron oxides/reduced graphene oxide (rGO) nanocomposites as the anode material for LIBs. The surface of GO contains more functional groups and provides more reaction sites for the adsorption of Fe^{3+} to form crystals [37]. The synthesized nano-scale iron oxide particles have a diameter of about 50 nm and evenly distributed on the rGO sheets. The introduction of rGO enhances the conductivity of the materials and accelerates the diffusion and transportation of Li^+ ions [38]. Therefore, the Fe_2O_3 cubes/rGO nanocomposites display the outstanding specific capacity, superior rate performance, and great cycle stability. Among them, Fe_2O_3-rGO-c0.2 shows the most excellent electrochemical properties, which exhibits the superior initial capacity of 1580.6 mAh g^{-1} with outstanding reversible capacity of 1145.4 mAh g^{-1} after 100 cycles at the current density of 200 mA g^{-1}. Otherwise, Fe_2O_3-rGO-c0.2 performs the superior rate performance of 708 mAh g^{-1} at 2000 mA g^{-1} and 479.1 mAh g^{-1} at 5000 mA g^{-1}. In addition, due to the well-designed structure, the composite exhibits pseudocapacitance-dominated storage behavior.

Experimental

Chemicals

The reagents adopted in this work, such as sodium acetate (CH_3COONa) and ferric chloride hexahydrate ($FeCl_3 \cdot 6H_2O$), were supplied by Shanghai Ling Feng Chemical Reagent Co. Ltd. GO were bought from Chengdu Organic Chemicals Co. Ltd.

Preparation of Fe_2O_3-reduced graphene oxide-cx

In the synthesis of Fe_2O_3-reduced graphene oxide-cx (Fe_2O_3-rGO-cx), GO is used as the carbon structure skeleton, ferric chloride hexahydrate is used as the iron source, and Fe_2O_3-rGO-cx composites with different carbon contents are synthesized by hydrothermal reaction. The detailed preparation method is as follows. First, a certain amount of GO was added to the breaker, and then, 50 ml deionized water was poured, subsequently sonicated for 1 h at room temperature to obtain the uniform brown suspension. Next, 1.5 mmol ferric chloride hexahydrate solid was added to 30 ml mixture solution (15 ml C_2H_5OH + 15 ml H_2O) under constant mechanical stirring until it was dissolved completely. Then, 4.6 mmol sodium acetate was dissolved into the mixed solution, with stirring for 20 min to obtain a brick red solution. Afterwards, above solution was injected to the GO suspension. Finally, the resulting solution was transferred to 100 ml Teflon autoclave, which was subsequently heated at 150 °C for 12 h. When it is cooled naturally to ambient temperature, centrifuged, and washed, the black powders were obtained, which were frozen in a refrigerator for 12 h and then dried in a freeze dryer for 24 h.

According to the theoretical mass ratio of GO to Fe_2O_3, the sample was named Fe_2O_3-rGO-cx ($x = 0.1, 0.2, 0.3, 0.4$). The synthesis of the pure Fe_2O_3 sample was consistent with the abovementioned experimental process without the addition of GO suspension. The obtained brick-red powder sample is named Fe_2O_3-cube.

Characterizations

The scanning electron microscopy (SEM, Gemini SEM 500) was adopted to analyze the morphologies with particle size of the nanocomposites, and the transmission electron microscopy was conducted to examine the internal structures and lattice fringes of the nanocomposites. The thermogravimetric analysis (TA instrument Q600) was performed to test the carbon contents in the nanocomposites, with an air flow of 100 ml min^{-1} and the heating rate 10 °C min^{-1} to 800 °C. Powder X-ray diffraction analysis was adopted to analyze the crystal form with the instrument of Rigaku D/max 2550 X-ray diffractometer. The test conditions are as follows: tube pressure was 40 kV, current was 20 mA, and Cu (Kα) radiation in the range of 10°–80°. The nanocomposites were characterized by Raman spectrometer using a Renishaw in Via Relfex with excitation source of an Ar laser ($\lambda = 514.5$ nm). The samples were first degassed at 120 °C for 12 h, and then tested in Quadrasorb SI analyzer to obtain nitrogen adsorption and desorption data. The surface chemistry of nanocomposites was tested by X-ray photoelectron spectroscopy (XPS) with the instrument of scientific ESCALab220i-XL. The excitation source was Al/Kα line, the operating voltage was 15 kV, the current was 10 mA, the power was 300 W, and the analysis chamber pressure was lower than 2×10^{-8} Torr.

Electrochemical tests

The prepared material was used as the anode material which was assembled in CR2016 coin cells for the electrochemical performance tests. The slurry is prepared by adding Fe_2O_3-rGO-cx or Fe_2O_3-cube, conductive agent (super C), and polyvinylidene fluoride to N-methyl pyrrolidone with a mass ratio of 8:1:1, then magnetic stirring for 12 h. Afterwards, the slurry is poured on the copper foil (mass loading ~ 1.0 mg cm^{-2}), which was moved into an oven at 80 °C for 6 h, and then further dried in the vacuum oven at 110 °C overnight. Subsequently, the sheet was punched into disk-type electrodes with a diameter of 12 mm. The as-prepared electrodes were used as the working electrodes. The electrolyte used the prepared solution which contained 1 M lithium hexafluorophosphate and the mixture solution of ethylene carbonate-dimethyl carbonate-ethyl carbonate (volume ratio

1:1:1). Celgard 2500 as the separator and the lithium plate as the reference electrode. Adopting the CR2016 shells to complete the battery assembly in the glove box with argon, which the water and oxygen were controlled within 1 ppm. The cyclic voltammetry (CV) curves of the battery were fulfilled in the workstation Arbin BT2000 with the scan rate which was controlled at 0.1 mV s^{-1}. The analysis of galvanostatic charge and discharge (GCD) acquired in the LAND CT2001A test system with the potential range of 0.01–3.0 V. Electrochemical impedance spectroscopy (EIS) tests were examined on the electrochemical workstation Gamry Reference 600 with the sinusoidal excitation voltage of 5.0 mV, with the frequency between 0.01 Hz and 100 kHz.

Results and discussion

Characterization of the Fe₂O₃-rGO-cx

The synthesis process of Fe_2O_3-rGO-cx is illustrated in Fig. 1. Since the surface of GO contains electronegative functional groups, the Fe^{3+} ions are adsorbed to the surface of GO through electrostatic interaction. The iron oxide crystal nucleus is fixed on the surface of GO after hydrothermal treatment; moreover, GO is reduced to rGO. Meanwhile, the functional groups on the GO surface which are not paired with the trivalent iron ions are removed during the hydrothermal process. Finally, high-temperature carbonization treatment is carried out to make the iron oxide crystal nuclei further grow.

In order to analyze the apparent morphology of Fe_2O_3-rGO-cx, SEM and TEM analyses are carried out, as shown in Fig. 2. It can be observed from Fig. 2a–d that the iron oxide nanoparticles exhibit the small cubic structure, with a size of about 50 nm. Moreover, the particles have a relatively regular shape and uniform size distribution. With different mass ratios, the size and morphology of the iron oxide particles remain unchanged, and the incalculable particles are evenly distributed and tightly integrated on the surface of rGO. In addition, the rGO in nanocomposites exhibits a typical wrinkled structure with large area which is beneficial to the adsorption of iron oxide. GO will be reduced to rGO which leads to its oxygen-containing functional groups reducing and surface defects increasing in the hydrothermal process. These defects provide more active sites which can be used for storage of lithium ions. With the increase of rGO, iron oxides on the surface of rGO show good dispersibility. The addition of rGO in nanocomposite enhances the conductivity of the electrode and effectively inhibits the volume expansion which caused by the iron oxide particles during the lithiation/de-lithiation. Otherwise, good structure of nanocomposites effectively alleviates the fragmentation and pulverization of the active electrode. The
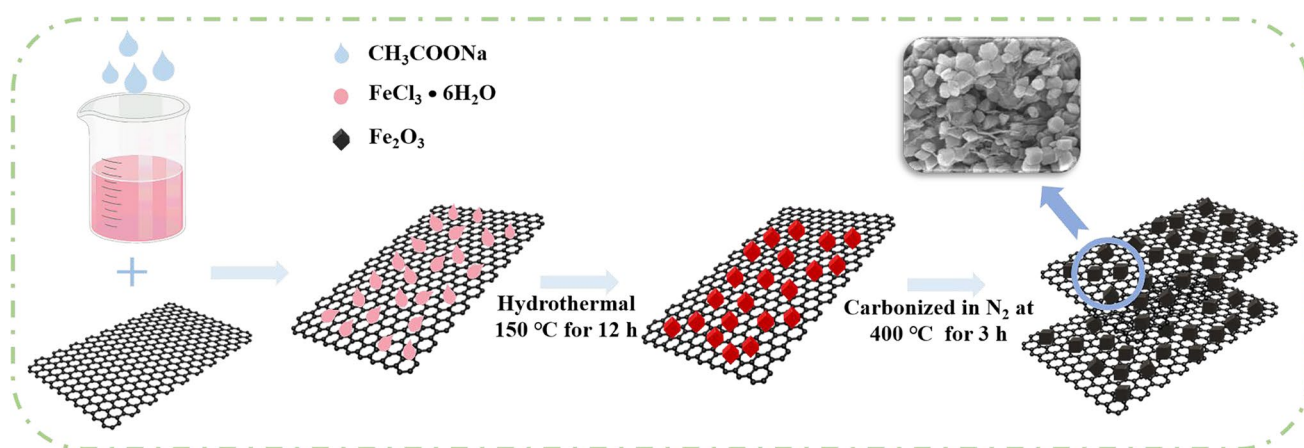
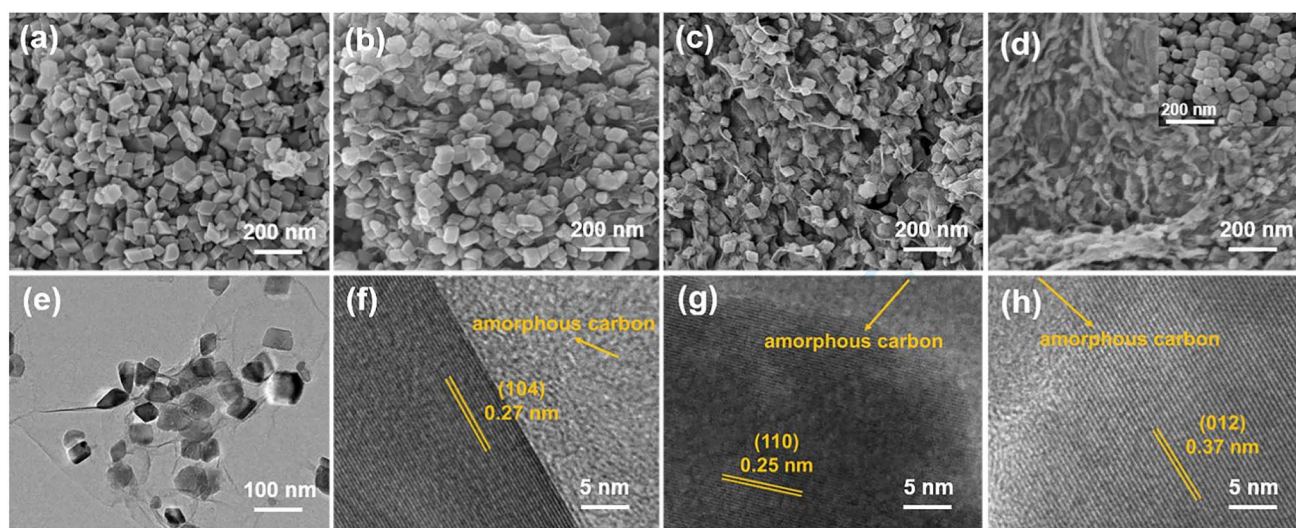**Fig. 1** Schematic illustration of the Fe_2O_3-rGO-cx composites

Fig. 2 SEM images of **a** Fe_2O_3-rGO-c0.1, **b** Fe_2O_3-rGO-c0.2, **c** Fe_2O_3-rGO-c0.3, and **d** Fe_2O_3-rGO-c0.4 (illustration is Fe_2O_3-cube); **e** TEM image and **f–h** HR-TEM images of Fe_2O_3-rGO-c0.2

TEM image further indicates that Fe_2O_3 cubes are evenly distributed on the surface of rGO sheets (Fig. 2e). A high-resolution TEM (HR-TEM) image demonstrates the lattice fringe spacings of 0.27 nm, 0.25 nm, and 0.37 nm, which matches with the (104), (110), and (012) crystal planes of α-Fe_2O_3 respectively. As shown in Fig. 2f, g, and h, the light part is amorphous carbon layer, and the dark part is α-Fe_2O_3 particle.

Thermogravimetric analysis is adopted to confirm the carbon and metal oxide content of the materials, the results are shown in Fig. 3a. The carbon contents in Fe_2O_3-rGO-cx ($x = 0.1, 0.2, 0.3, 0.4$) are 7.6%, 10.3%, 15.2%, and 17.2%; therefore, the metal oxide contents are 91.4%, 88.7%, 83.8%, and 81.8%. Fe_2O_3-rGO-cx nanocomposites show similar thermal stability. In the initial stage, the evaporation of water brings a small amount of weight loss, and the main loss

between 300 and 500 °C is resulted from the combustion of rGO. When the temperature exceeds 500 °C, the curve shows a slight weight loss, which corresponds to the trace mass decrease of the sample being taken away by the air flow. The thermal weight loss behavior of Fe_2O_3-rGO-c0.2 can clearly observe from the differential thermal analysis which is shown in Fig. 3b.

Otherwise, XRD analysis is conducted to explore the components of the Fe_2O_3-rGO-cx (as shown in Fig. 3c). The XRD results of Fe_2O_3-cube and Fe_2O_3-rGO-c0.2 are consistent with the standard patterns of α-Fe_2O_3 (PDF: 87–1166). Meanwhile, the peaks are sharp and obvious, indicating that the composite has a complete α-Fe_2O_3 crystal phase. The diffraction peaks at 24.2°, 33.1°, 35.6°, 40.8°, 49.5°, 54.1°, 57.6°, 62.5°, 64.0°, 71.9°, and 75.5° correspond to the (012) (104) (110) (113) (024) (116) (122) (214) (300) (119) (220)

Fig. 3 **a** TG curves of Fe_2O_3-rGO-cx and Fe_2O_3-cube in air, **b** the differential thermal analysis of Fe_2O_3-rGO-c0.2, **c** XRD patterns of Fe_2O_3-cube and Fe_2O_3-rGO-c0.2, and **d** Raman spectrum patterns of Fe_2O_3-rGO-cx
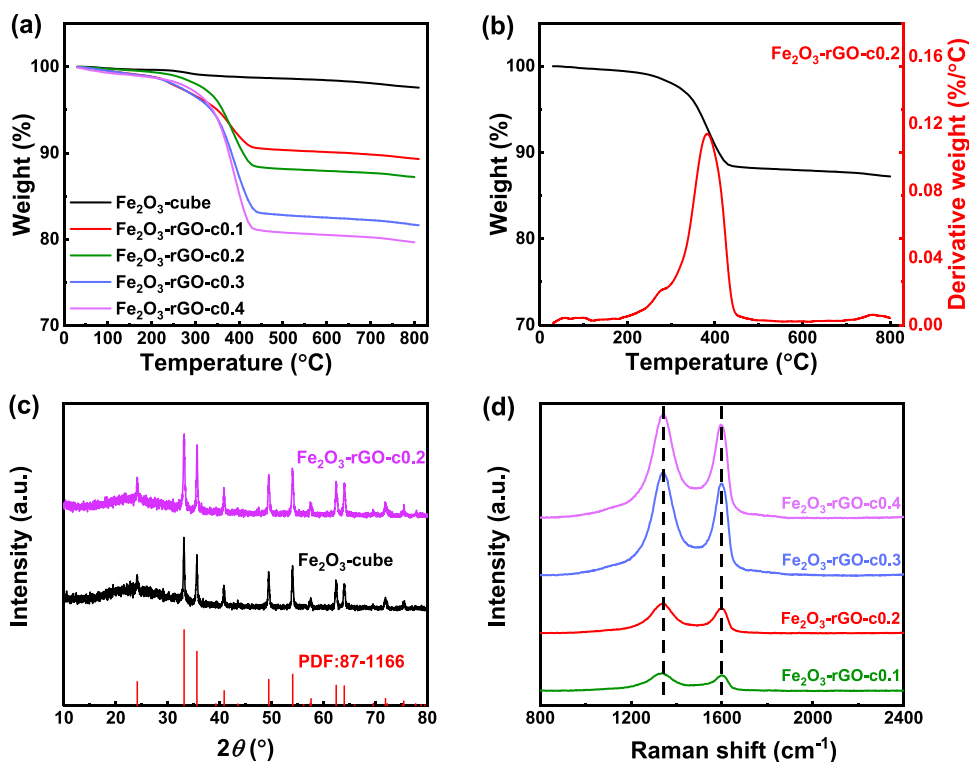
crystalline planes of α-Fe_2O_3 respectively [39]. The conclusion is consistent with the result obtained by TEM. Raman spectroscopy analysis (Fig. 3d) is used to detect the structure of carbon in Fe_2O_3-rGO-cx. The result further proves the existence of rGO in nanocomposites, in which two obvious scattering peaks are observed corresponding to G and D bands at 1342 cm^{-1} and 1600 cm^{-1}. Comparing with the original graphite, the positions of two bands are shifted [40]. Meanwhile, it can be found that with the increase of the rGO, the peak intensity is increasing. The I_D/I_G value of GO is 0.63, while Fe_2O_3-rGO-c0.1, Fe_2O_3-rGO-c0.2, Fe_2O_3-rGO-c0.3, and Fe_2O_3-rGO-c0.4 are 1.135, 1.054, 1.052, and 1.045 respectively. The higher intensity ratio of D/G indicates which samples have the more disordered graphene and defects. It is beneficial to capture electrons and effectively improve the conductivity. Furthermore, it is conducive to transport electrons and ions, and even provides more active sides for lithium-ion storage.

In order to detect the porosity of five nanocomposites, the experiment of N_2 adsorption/desorption was conducted. All isotherms (Fig. 4a) have symbolic hysteresis loops, which illustrates the nanocomposites possessing mesoporous structure. Meanwhile, the specific surface area of Fe_2O_3-cube is 28.3 m^2 g^{-1}; Fe_2O_3-rGO-cx ($x = 0.1, 0.2, 0.3, 0.4$) are 63.2, 91.2, 117.4, and 132.6 m^2 g^{-1}, respectively (Table 1 is the detailed data). It can be noticed that the specific surface area is effectively improved, with the addition of rGO the specific

surface area increasing. However, the pore volume shows the trend of increasing and then decreasing with the increase of rGO. From Fig. 4b, it can be found that the mesopores of nanocomposites are mainly concentrated at 4 nm. The appropriate pore structures are greatly conducive to improve the transportation of lithium ions and electrons and promote the rapid infiltration of electrolyte.

The chemical composition and valence state of nanocomposites were determined by XPS. Figure 4c is the full XPS spectra of Fe_2O_3-cube and Fe_2O_3-rGO-c0.2, which proving the existence of Fe, O, and C elements. Figure 4d shows the high-resolution C 1 s XPS split peak fitting spectrum, which demonstrates C 1 s spectra of Fe_2O_3-rGO-c0.2 possessing C–C/C=C group at 284.7 eV, C–O bond at 285.7 eV and O-C=O group at 288.7 eV. The peaks in the O 1 s spectrum (Fig. 4e) correspond to the C=O, C-O-Fe, and C–OH/C–O–C groups with the binding energy at 530.9 eV, 531.8 eV, and 533.9 eV, respectively. The C-O-Fe bond indicates a strong connecting structure between rGO and Fe_2O_3, which shows the Fe_2O_3 is well anchored on the rGO sheets. The C–OH/C–O–C bond reflects the characteristic oxygen-containing functional groups of rGO and illustrates the stacking structure of nanocomposites. The two peaks in Fe 2p spectrum (Fig. 4f) are assigned as the Fe $2p_{3/2}$ and Fe $2p_{1/2}$ with the energy of 711.5 eV and 725.1 eV. Moreover, it is accompanied by two small satellite peaks at 718.9 eV and 732.1 eV, which matches well with the typical binding energy of Fe_2O_3 [41].

Fig. 4 **a** N$_2$ adsorption–desorption isotherm profiles and **b** BJH pore size distribution of Fe$_2$O$_3$-cube and Fe$_2$O$_3$-rGO-cx. XPS spectra: **c** full spectra of Fe$_2$O$_3$-cube and Fe$_2$O$_3$-rGO-c0.2 and **d** C 1 s spectra, **e** O 1 s spectra, and **f** Fe 2p spectra of Fe$_2$O$_3$-rGO-c0.2
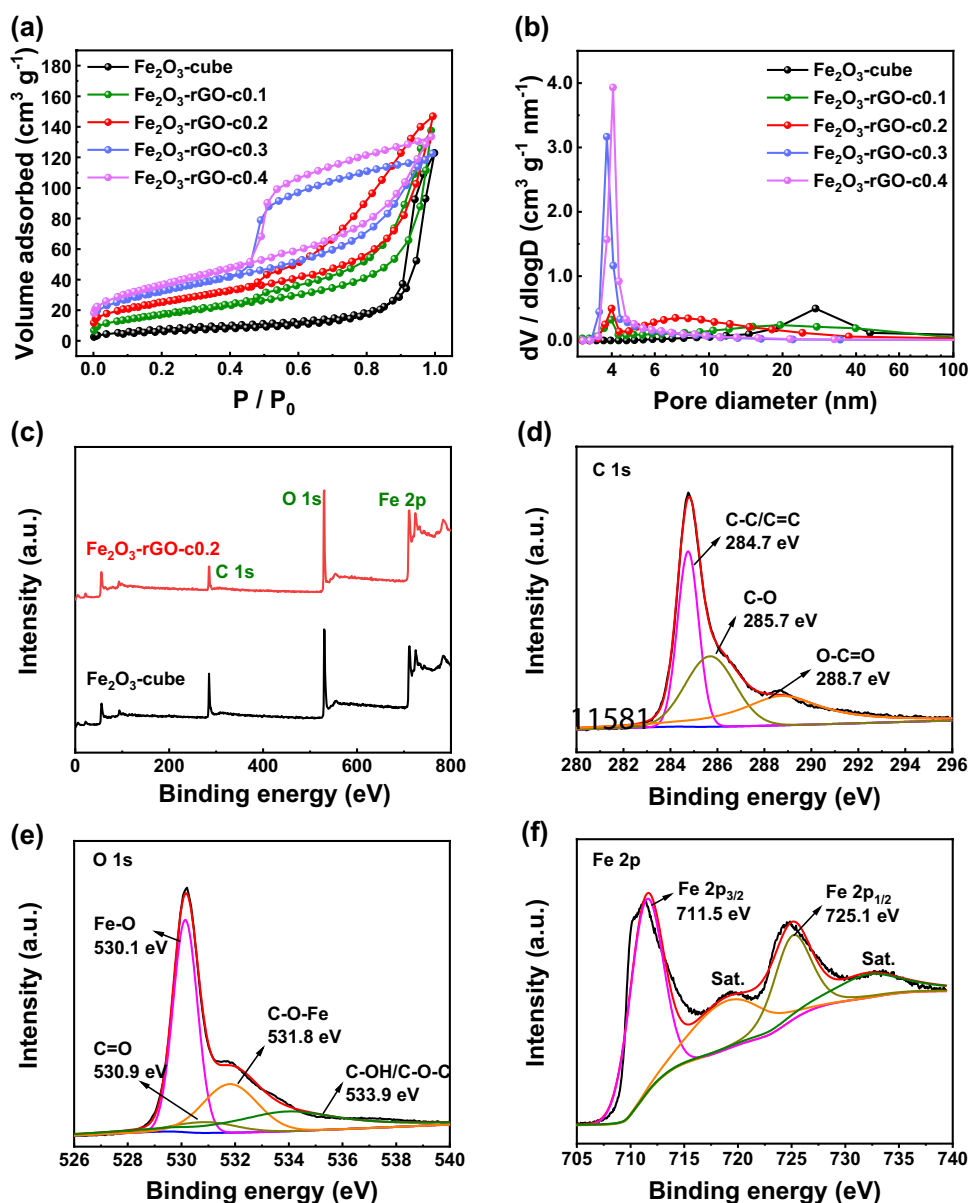

Table 1 The pore parameters of Fe$_2$O$_3$-cube, Fe$_2$O$_3$-rGO-c0.1, Fe$_2$O$_3$-rGO-c0.2, Fe$_2$O$_3$-rGO-c0.3, and Fe$_2$O$_3$-rGO-c0.4

Nanocomposite	S_{BET}[a] m^2 g^{-1}	V_T[b] cm^3 g^{-1}
Fe$_2$O$_3$-cube	28.3	0.19
Fe$_2$O$_3$-rGO-c0.1	63.2	0.21
Fe$_2$O$_3$-rGO-c0.2	91.2	0.23
Fe$_2$O$_3$-rGO-c0.3	117.4	0.19
Fe$_2$O$_3$-rGO-c0.4	132.6	0.21

[a]S_{BET}, specific surface area; [b]V_T, total pore volume ($P/P_0 = 0.99$)

Electrochemical performance

Electrochemical measurements are carried out for the purpose of inspecting the electrochemical properties of the five nanocomposites. The CV curves are obtained at a scan rate of 0.1 mV s^{-1}, with the results are evaluated in Fig. 5a–b. Two small cathode peaks at 1.65 V and 1.00 V can be detected in the first scan, which are attributed to the irreversible reaction. It causes by electrolyte decomposition and lithium ions intercalating into α-Fe$_2$O$_3$ to form Li$_x$Fe$_2$O$_3$. Otherwise, a main peak is found at 0.70 V, this is because the Fe^{3+} is reduced to Fe^{2+} and further reduced to Fe^0; moreover, it also includes the factor in the fabrication of the solid electrolyte interphase (SEI) layer [42]. The reaction at the anode is just opposite to cathode; therefore, it occurs the

Fig. 5 Cycling voltammetry profiles of **a** Fe_2O_3-cube and **b** Fe_2O_3-rGO-c0.2; charging-discharging profiles of **c** Fe_2O_3-cube and **d** Fe_2O_3-rGO-c0.2
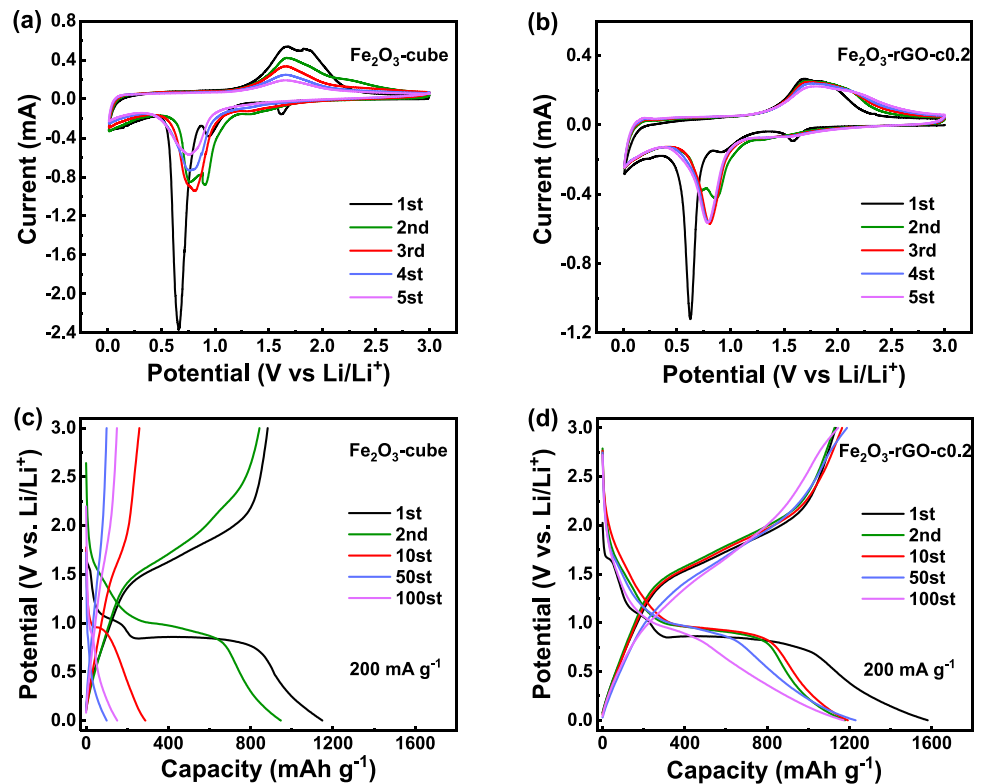
oxidation of Fe^0 to Fe^{2+} and Fe^{3+} at 1.67–1.88 V. Starting from the subsequent scans, the reduction peaks located at 1.65 V and 1.00 V disappeared, with the other peaks reduced and shifted to a certain extent. This is due to the SEI layer and electrode polarization, which leads to the reduction of peak intensity and the shift of peak position. Meanwhile, by comparing the existence of rGO, it can be found that the reversibility of material combination with rGO is better than the Fe_2O_3-cube.

The charge/discharge profiles (Fig. 5c–d) of Fe_2O_3-cube and Fe_2O_3-rGO-c0.2 with different cycles were measured at the current density of 200 mA g^{-1}. All curves exhibit a stable discharge platform at 0.83 V (vs Li/Li$^+$) which is mainly related to the process of Li$^+$ inserting into α-Fe_2O_3 to generate $Li_xFe_2O_3$ and Fe^{3+} reduction to Fe^0. The charge platform at 1.85 V is assigned as the oxidation process from Fe^0 to Fe^{3+}. For Fe_2O_3-rGO-c0.2, the charge capacity is 1133.8 mAh g^{-1} and the discharge capacity is 1580.6 mAh g^{-1} in the primary cycle, which are significantly better than Fe_2O_3-cube (883.0 mAh g^{-1} and 1148.4 mAh g^{-1}). It can be found that the initial discharge capacity of Fe_2O_3-rGO-c0.2 is higher than the theoretical value of Fe_2O_3, which may be caused by the following reasons. First, the formation of rGO after hydrothermal supplies more defects to store extra lithium ions. Second, the formation of SEI film on the surface of electrodes consumes excessive lithium ions during the first cycle. Third, the decomposition of the electrolyte provides part of lithium ions. Subsequently, with the

increase of cycles, the capacity decay rate shows a slowing trend. The addition of rGO effectively avoids the capacity attenuation, therefore, the Fe_2O_3-rGO-c0.2 shows good cycle reversibility. The appropriate addition of rGO makes the carbon-based support with the iron oxide to present a good synergistic effect, which leads to the conductivity and stability significantly improve. The phenomenon that the reversible capacity of the 100th cycle is greater than the 50th cycle in nanocomposites as a result of the incomplete contact between the active material and the electrolyte at the beginning. Afterwards, the electrolyte infiltrates electrode completely and the material is slowly activated, therefore, the specific capacity is fully utilized.

In order to further explore the capability of the nanocomposites, the cycle stability performance tests are carried out at a current of 200 mA g^{-1} (the results displayed in Fig. 6a). The material combination with rGO shows excellent stability. The initial discharge capacity of Fe_2O_3-rGO-c0.2 reaches 1580.6 mAh g^{-1}, and still maintains the 1145.4 mAh g^{-1} after 100 cycles, which is significantly better than Fe_2O_3-cube (151.4 mAh g^{-1}), Fe_2O_3-rGO-c0.1 (974.6 mAh g^{-1}), Fe_2O_3-rGO-c0.3 (1041.9 mAh g^{-1}), and Fe_2O_3-rGO-c0.4 (854.7 mAh g^{-1}). There is less rGO in Fe_2O_3-rGO-c0.1, and the capacity attenuation is serious in the initial stage. With the activation of iron oxide combined the lithium storage in rGO, the capacity gradually increases in the later stage. Fe_2O_3-rGO-c0.2 contains a proper amount of rGO, the capacity shows a slight upward trend. Due to

Fig. 6 **a** Cycling performance at the current of 200 mA g^{-1}, **b** rate performance at various current densities from 0.1 to 5 A g^{-1}, **c** coulombic efficiencies, and **d** EIS profiles of five nanocomposites
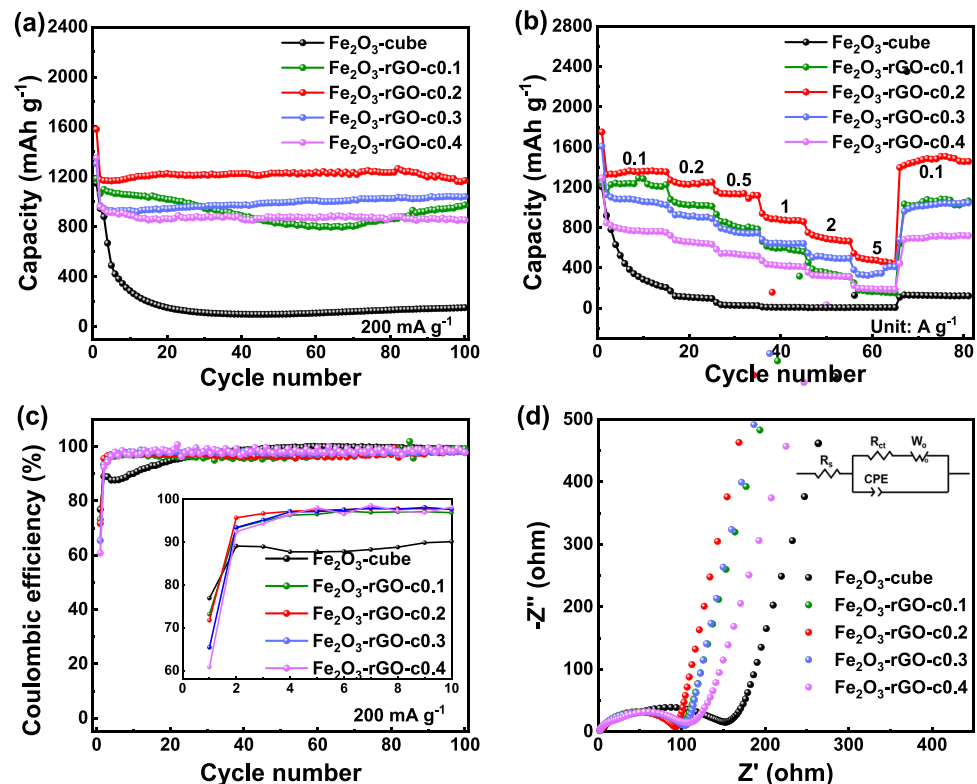
excessive rGO in Fe$_2$O$_3$-rGO-c0.3 and Fe$_2$O$_3$-rGO-c0.4, the capacities are relatively lower. The result confirms the appropriate addition of rGO helps to increase the specific capacity, and the optimal mass ratio of Fe$_2$O$_3$ with GO is 1:0.2. In addition, excessive rGO will reduce the specific capacity and volumetric energy density of the entire electrode, and hinder its practical application.

Figure 6b demonstrates the rate performance profiles with the different hybrids at the current of 0.1, 0.2, 0.5, 1, 2, and 5 A g^{-1}. The capacity of pure Fe$_2$O$_3$-cube is less than 10 mAh g^{-1} at the current of 1, 2, and 5 A g^{-1}. However, the nanocomposites combined with rGO show excellent stability at different magnifications. After different magnification tests, the current density rises back to the initial value, capacity also returns to the initial capacity. This is owing to the excellent structure of the graphene encapsulation which provides the ability to withstand large currents. Fe$_2$O$_3$-rGO-c0.2 exhibits the best capacities of 1360.6, 1199.3, 1112.1, 877.3, 689.4, and 479.4 mAh g^{-1} at different current densities, then restores to 1439.4 mAh g^{-1} at 0.1 A g^{-1}. The outstanding electrochemical performance of Fe$_2$O$_3$-rGO-c0.2 is significantly better than current iron-based materials (refer to Table 2 for comparison information) [43–47]. As the content of rGO increases, the conductivity of the sample increases, but Fe$_2$O$_3$-rGO-c0.3 and Fe$_2$O$_3$-rGO-c0.4 show poor rate performance. This is because excessive rGO leads to a decrease in the lithium storage capacity. It is clarified that the introduction of appropriate rGO into the materials

can effectively promote the reversibility and stability. The coulombic efficiencies are shown in Fig. 6c. The initial coulombic efficiency of the Fe$_2$O$_3$-rGO-c0.2 (71.73%) is lower than Fe$_2$O$_3$-cube (76.89%), because of its larger specific surface area which results in more consumption of lithium ions during the formation of SEI film. Due to the stable SEI film, Fe$_2$O$_3$-rGO-c0.2 shows better stability in subsequent cycles. As the content of rGO in the nanocomposites increases, the initial coulombic efficiency decreases slightly; the order of efficiency is as follows: Fe$_2$O$_3$-rGO-c0.1 (73.14%) > Fe$_2$O$_3$-rGO-c0.2 (71.73%) > Fe$_2$O$_3$-rGO-c0.3 (65.41%) > Fe$_2$O$_3$-rGO-c0.4 (60.82%). With the increase of rGO, the specific surface area of the material also increases

Table 2 Comparison of the electrochemical properties of Fe$_2$O$_3$-rGO-c0.2 with other reported Fe$_2$O$_3$-based nanocomposites

Composite	Cycle capacity/ cycle number/current density (mAh g^{-1}/ cycles/A g^{-1})	Rate capacity/ current density (mAh g^{-1}/A g^{-1})	Reference
Fe$_2$O$_3$-C–Ag	858/200/0.1	515/1	[43]
Fe$_2$O$_3$@C/CC	1091/100/0.2	507/1	[44]
α- Fe$_2$O$_3$@C(CSNR)	920/200/0.5	392/5	[45]
Fe$_3$O$_4$/C	1300/100/0.1	900/1	[46]
Fe$_2$O$_3$@C	1013/80/0.2	710/2	[47]
Fe$_2$O$_3$-rGO-c0.2	1145.4/100/0.2	479.1/5	This work

(shown in Table 1), and the formation of a stable SEI film consumes more lithium ions, resulting in a slight decrease in the coulombic efficiency. However, the efficiencies gradually rise during the first 5 cycles, and basically reach 95–100% in the fifth cycle. In contrast, pure Fe_2O_3-cube needs 20 cycles to reach the stability, which is consistent with the result of GCD.

In order to further understand the diffusion behavior of lithium ions and the influence of rGO on the conductivity, the EIS tests of the Fe_2O_3-cube and the Fe_2O_3-rGO-cx nanocomposites were carried out. Figure 6d is the EIS curves and the analog equivalent circuit. Rs represents the ohmic contact impedance. CPE stands for the electric double layer capacitance in the electrode. Rct means the charge transfer impedance and the value corresponds to the size of semicircle diameter, which directly reflects the main resistance of the electrode and has a greater impact on transportation of Li^+ and electrons. Wo means the WarBurg impedance and the value equal to the slope of oblique line, which can reflect the migration rate of Li^+ [46]. The value of Fe_2O_3-cube is 158.5 Ω which is larger than the composites of Fe_2O_3-rGO-cx, indicating the Fe_2O_3 combined with rGO enhances the conductivity of the materials. Among the nanocomposites, Fe_2O_3-rGO-c0.2 has the smallest semicircle diameter, which means it has the lowest Rct (92.33 Ω). Meanwhile, the Rct of Fe_2O_3-rGO-c0.1, Fe_2O_3-rGO-c0.3, and Fe_2O_3-rGO-c0.4 is 96.15 Ω, 101.70 Ω, and 115.20 Ω

respectively. Comparing the values of different composites, it can be found that the Rct of Fe_2O_3-rGO-cx is significantly lower than Fe_2O_3-cube. It shows that the addition of rGO accelerates the transportation and diffusion of Li^+ ions and improves the electrochemical performance of the materials.

The composite exhibits excellent electrochemical performance, and to further investigate the reasons for this, the Fe_2O_3-rGO-c0.2 material was selected to perform CV tests at different scan rates (Fig. 7a). The lithium-ion storage behaviors mainly include diffusion-controlled and capacitance-controlled, and the storage mechanism can be analyzed by the relationship between the peak current (*i*) and the scan rate (*v*) (Eq. 1–2) [14, 48]:

$$i = av^b \tag{1}$$

$$\log i = b \log v + \log a \tag{2}$$

the *a* and *b* in the equations are adjustable parameters. The value of *b* close to 0.5 indicates that diffusion-controlled mechanism is the main reason. When the value of *b* is close to 1, it suggests that the behavior is capacitive control. It can be seen from Fig. 7b that *b* values of the reduction and oxidation peaks in Fe_2O_3-rGO-c0.2 are 0.8098 and 0.9513, respectively, indicating that the sample is mainly controlled by the capacitive behavior.

Fig. 7 **a** Cycling voltammetry profiles at various scan rates, **b** values of *b* at oxidation peak and reduction peak, **c** capacitive contribution (red region) at scan rate of 1 mV s^{-1}, and **d** ratios of capacitance and diffusion contribution at different scan rates for Fe_2O_3-rGO-c0.2
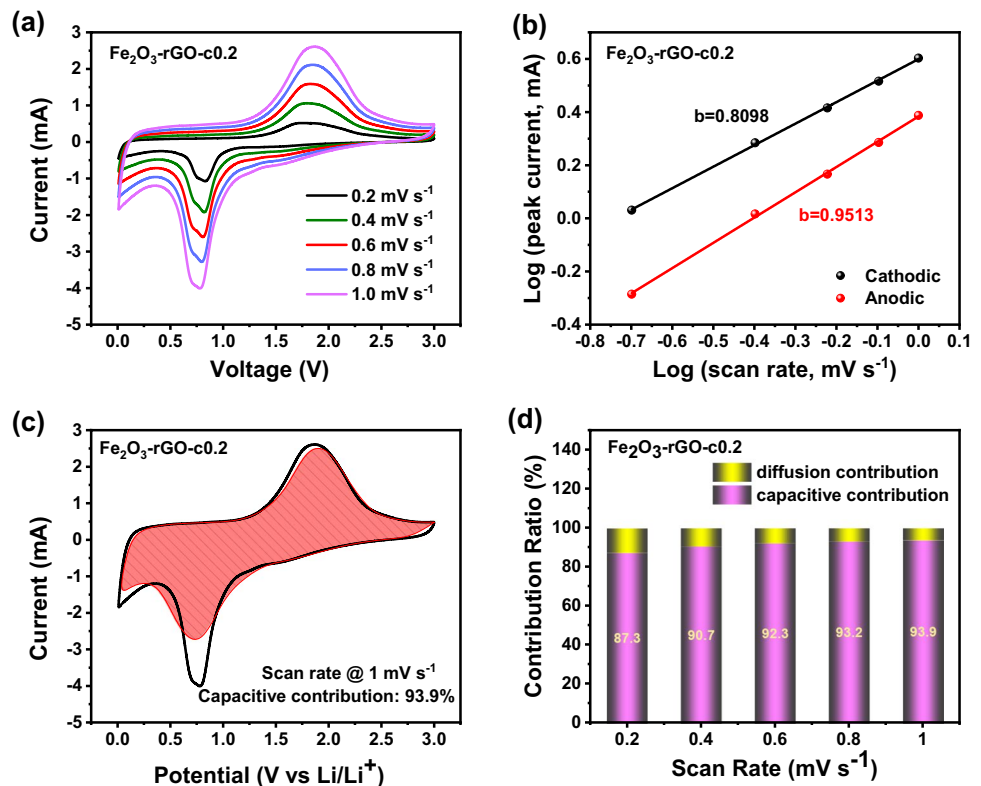
In order to further quantify the contribution of the capacitive behavior to the total capacity at a fixed scan rate, the total capacity can be decomposed into two parts, the capacitive contribution and the diffusion-controlled contribution, which are calculated according to the following equations [7, 49]:

$$i(V) = k_1 v + k_2 v^{1/2} \tag{3}$$

$$i(V)/v^{1/2} = k_1 v^{1/2} + k_2 \tag{4}$$

where k_1 and k_2 are constants. By calculating the slope of the $i/v^{1/2} \sim v^{1/2}$ curve, the capacitance current ($k_1 v$) and the capacitance contribution percentage are obtained, as shown in Fig. 7c–d. As the scan rate increases, the percentage of capacitive contribution increases gradually. When the scan rate increases to 1 mV s^{-1}, the capacitance contribution is as high as 93.9%, indicating that capacitive storage plays a key role in the total capacity of the electrode. The greater the contribution of the pseudocapacitive effect to the composite electrode, the more favorable it is for LIBs to achieve fast charge storage at high current densities, thereby achieving a high battery capacity.

Conclusion

In conclusion, the nanocomposites Fe$_2$O$_3$-rGO-cx are prepared by the simple hydrothermal method, which exhibits excellent electrochemical performance. Particularly, Fe$_2$O$_3$-rGO-c0.2 shows superior capacity performance (1145.4 mAh g^{-1} at 200 mA g^{-1}), high coulombic efficiencies (~ 100%), outstanding rate capability (479 mAh g^{-1} at 5000 mA g^{-1}), and the capacitive control behavior as high as 93.9% when the scan rate is 1 mV s^{-1}. The reasons for the high performance of the Fe$_2$O$_3$-rGO-c0.2 are summarized as follows: (1) the preparation of nanostructured iron oxide allows the particles to undergo relatively small volume changes during the process of lithiation/de-lithiation, so that the nanocomposites could maintain the structural integrity. Elaborated nanostructure ensures the good contact between the active material and electrolyte. (2) The rGO provides high conductivity and good mechanical flexibility; therefore, the nanocomposites possess outstanding electrical conductivity. Moreover, the iron oxide particles are confined in the graphene layer, which avoids the agglomeration of iron oxide and the stacking of rGO layers. In addition, more functional groups and defects on the surface of rGO offer active sites to store lithium ions. (3) Nanocomposites can provide the suitable channels to transport lithium ions and electrons. Moreover, it has a certain buffer capacity for the expansion of the iron oxide particles which solves the problem of pulverization and shedding of the electrodes. In this paper, the preparation of monodispersed Fe$_2$O$_3$ cubes/rGO nanocomposite is simple, which has good application prospects in lithium-ion battery.

Declarations

Consent for publication This manuscript is approved by all authors for publication.

Competing interests The authors declare no competing interests.

References

1. Huang Y, Lin Z, Zheng M, Wang TH, Yang JZ, Yuan FS, Lu XY, Liu L, Sun DP (2016) Amorphous Fe$_2$O$_3$ nanoshells coated on carbonized bacterial cellulose nanofibers as a flexible anode for high-performance lithium ion batteries. J Power Sources 307:649–656

2. Almodóvar P, López ML, Ramírez-Castellanos J, Nappini S, Magnano E, José MG, Carlos D-G (2021) Synthesis, characterization and electrochemical assessment of hexagonal molybdenum trioxide (h-MoO$_3$) micro-composites with graphite, graphene and graphene oxide for lithium ion batteries. Electrochim Acta 365: 137355.

3. Hu J, Zheng J, Tian L, Duan YD, Lin LP, Cui SH, Peng H, Liu TC, Guo H, Wang XW, Pan F (2015) A core-shell nanohollow-γ-Fe$_2$O$_3$@graphene hybrid prepared through the Kirkendall process as a high performance anode material for lithium ion batteries. Chem Commun 51(37):7855–7858

4. Ju W, Dong C, Jin B, Zhu YF, Wen Z, Jiang Q (2020) Composites of reduced graphene oxide and Fe$_2$O$_3$ nanoparticles anchored on MoS$_2$ nanosheets for lithium storage. ACS Appl Nano Mater 3(9):9009–9016

5. Zhu X, Song X, Ma X, Ning GQ (2014) Enhanced electrode performance of Fe$_2$O$_3$ nanoparticle-decorated nanomesh graphene as anodes for lithium-ion batteries. ACS Appl Mater Interfaces 6(10):7189–7197

6. Li WW, Peng J, Li H, Wu ZY, Huang YH, Chang BB, Guo XW, Chen GR, Wang XY (2021) Encapsulating nanoscale silicon inside carbon fiber as flexible self-supporting anode material for lithium-ion battery. ACS Appl Energy Mater 4:8529–8537

7. Jin XY, Li YW, Jiang JQ, Xiao SH, Yang JW, Yao JH (2021) Facile synthesis of monodispersed α-Fe$_2$O$_3$ cubes as a high-performance anode material for lithium-ion batteries. Ionics 27:3291–3299

8. Zhang Z, Liang J, Zhang X, Yang WF, Dong XL, Jung YG (2020) Dominant pseudocapacitive lithium storage in the carbon-coated ferric oxide nanoparticles (Fe$_2$O$_3$@C) towards anode materials for lithium-ion batteries. Int J Hydrog Energy 45(15):8186–8197

9. Fu Y, Zhou H, Hu Z, Yin S, Zhou LM (2020) Temperature-induced microstructure optimization of Co$_3$O$_4$ for the achievement of a high-areal-capacity carbon cloth-based lithium ion battery anode. Compos Commun 22: 100446

10. Zhu Y, Huang Y, Wang M, Wang K, Yu M, Chen XF, Zhang Z (2018) Novel carbon coated core-shell heterostructure NiCo$_2$O$_4$@NiO grown on carbon cloth as flexible lithium-ion battery anodes. Ceram Int 44(17):21690–21698

11. Kwon KM, Kim IG, Lee K-Y, Kim HS, Kim MS, Cho WI, Choi JY, Nah IW (2019) α-Fe$_2$O$_3$ anchored on porous N doped carbon derived from green microalgae via spray pyrolysis as anode materials for lithium ion batteries. J Ind Eng Chem 69:39–47

12. Lee KS, Park S, Lee W, Yoon YS (2016) Hollow nanobarrels of alpha-Fe$_2$O$_3$ on reduced graphene oxide as high-performance anode for lithium-ion batteries. ACS Appl Mater Interfaces 8(3):2027–2034

13. Zhu X, Zhu Y, Murali S, Stoller MD, Ruoff RS (2011) Nano-structured reduced graphene oxide Fe$_2$O$_3$ composite as a high-performance anode material for lithium ion batteries. ACS Nano 5(4):3333–3338

14. Huang Y, Li YW, Huang RS, Ji JC, Yao JH, Xiao SH (2021) One-pot hydrothermal synthesis of N-rGO supported Fe$_2$O$_3$ nanoparticles as a superior anode material for lithium-ion batteries. Solid State Ionics 368: 115693

15. Jiang T, Bu F, Feng X, Shakir I, Hao GL, Xu YX (2017) Porous Fe$_2$O$_3$ nanoframeworks encapsulated within three-dimensional graphene as high-performance flexible anode for lithium-ion battery. ACS Nano 11(5):5140–5147

16. Liu H, Luo S-H, Hu D-B, Liu X, Wang Q, Wang ZY, Wang YL (2019) Design and synthesis of carbon-coated α-Fe$_2$O$_3$@Fe$_3$O$_4$ hetero-structured as anode materials for lithium ion batteries. Appl Surf Sci 495: 143590

17. Ren Z, Yu S, Han B, Shao ZC, Wang ZY (2020) One-pot carbonization synthesis of γ-Fe$_2$O$_3$/Fe/carbon composite for high Li-storage and excellent stability. Mater Lett 275: 128066

18. Zhang G, Shi Y, Wang H, Jiang LL, Yu XD, Jing SY, Xing SX, Tsiakaras P (2019) A facile route to achieve ultrafine Fe$_2$O$_3$ nanorods anchored on graphene oxide for application in lithium-ion battery. J Power Sources 416:118–124

19. Jin XY, Li YW, Jin TF, Jiang JQ, Zhu Q, Yao JH (2022) Facile and efficient synthesis of binary FeOOH/Fe$_2$O$_3$ composite as a high-performance anode material for lithium-ion batteries. J Alloys Compd 896: 163026

20. Huang J-L, Fan L-Q, Gu Y, Nie YM, Yan J (2019) One-step solvothermal synthesis of high-capacity Fe$_3$O$_4$/reduced graphene oxide composite for use in Li-ion capacitor. J Alloys Compd 788:1119–1126

21. Wu C, Zhang H, Wu Y-X, Zhuang QC, Tian LL, Zhang XX (2014) Synthesis and characterization of Fe@Fe$_2$O$_3$ core-shell nanoparticles/graphene anode material for lithium-ion batteries. Electrochim Acta 134:18–27

22. Li LB, Shan YH (2021) The use of graphene and its composites to suppress the shuttle effect in lithium-sulfur batteries. New Carbon Mater 36(2):336–349

23. Tan Y, Zhu K, Li D, Bai F, Wei YJ, Zhang P (2014) N-doped graphene/Fe-Fe$_3$C nano-composite synthesized by a Fe-based metal organic framework and its anode performance in lithium ion batteries. Chem Eng J 258:93–100

24. Wang Q, Liu YD, Zhu GJ, Tang C, Sun WW, Du AJ, Wu MH, Zhang HJ (2021) Sn^{2+}-regulated synthesis of a bone-like Fe$_3$O$_4$@N-doped carbon composite as the anode for high-performance lithium storage. ACS Appl Energy Mater 4:3785–3793

25. Zhu Y, Zhang S, Sun Y, Xie AJ, Shen YH (2019) A novel FeC$_2$O$_4$-TOP derived porous pillar-like γ-Fe$_2$O$_3$/carbon nanocomposite with excellent performance as anode for lithium-ion batteries. Appl Surf Sci 479:1212–1219

26. Joshi B, Lee J-G, Samuel E (2017) Supersonically blown reduced graphene oxide loaded Fe-Fe$_3$C nanofibers for lithium ion battery anodes. J Alloys Compd 726:114–120

27. Luo G, Lu Y, Zeng S, Zhang SB, Yu XY, Fang YP, Sun LY (2015) Synthesis of rGO-Fe$_3$O$_4$-SnO$_2$-C quaternary hybrid mesoporous nanosheets as a high-performance anode material for lithium ion batteries. Electrochim Acta 182:715–722

28. Zhou G-W, Wang J, Gao P, Yang XW, He YS, Liao XZ, Yang J, Ma ZF (2012) Facile spray drying route for the three-dimensional graphene-encapsulated Fe$_2$O$_3$ nanoparticles for lithium ion battery anodes. Ind Eng Chem Res 52(3):1197–1204

29. Ma J, Kong Y, Liu S, Li YT, Jiang JB, Zhou QY, Huang YS, Han S (2020) Flexible phosphorus-doped graphene/metal-organic framework-derived porous Fe$_2$O$_3$ anode for lithium-ion battery. ACS Appl Energy Mater 3(12):11900–11906

30. Xia G, Li N, Li D (2013) Graphene/Fe$_2$O$_3$/SnO$_2$ ternary nanocomposites as a high-performance anode for lithium ion batteries. ACS Appl Mater Interfaces 5(17):8607–8614

31. Lian XB, Cao MC, Qin LL, Cao Y, Wu QH (2016) Synthesis of hierarchical nanospheres Fe$_2$O$_3$/graphene composite and its application in lithium-ion battery as a high-performance anode material. Ionics 22:2015–2020

32. Qi X, Zhang HB, Xu J, Wu XY, Yang DZ, Qu J, Yu ZZ (2017) Highly efficient high-pressure homogenization approach for scalable production of high-quality graphene sheets and sandwich-structured alpha-Fe$_2$O$_3$/graphene hybrids for high-performance lithium-ion batteries. ACS Appl Mater Interfaces 9(12):11025–11034

33. Sun Z, Fang S, Hu YH (2020) 3D graphene materials: from understanding to design and synthesis control. Chem Rev 120(18):10336–10453

34. Qin G, Ding L, Zeng M, Zhang KB, Zhang YQ, Bai Y, Wen JW, Li J (2020) Mesoporous Fe$_2$O$_3$/N-doped graphene composite as an anode material for lithium ion batteries with greatly enhanced electrochemical performance. J Electroanal Chem 866: 114176

35. Cao Y, Zhang A-Q, Zhang H, Ding GQ, Zhang LS (2020) A facile route to achieve Fe$_2$O$_3$ hollow sphere anchored on carbon nanotube for application in lithium-ion battery. Inorg Chem Commun 111: 107633.

36. Chen Y, Yuan X, Yang C, Lian YB, Razzaq AA, Hah RA, Guo J, Zhao XH, Peng Y, Deng Z (2019) γ-Fe$_2$O$_3$ nanoparticles embedded in porous carbon fibers as binder-free anodes for high-performance lithium and sodium ion batteries. J Alloys Compd 777:127–134

37. Yang L, Wu Y, Wu Y, Younas W, Jia J, Cao CB (2019) Hierarchical flower-like Fe$_2$O$_3$ mesoporous nanosheets with superior electrochemical lithium storage performance. J Energy Storage 23:363–370

38. Zhao Q, Liu J, Li X, Li XX, Xia ZZ, Zhang QX (2019) Graphene oxide-induced synthesis of button-shaped amorphous Fe$_2$O$_3$/rGO/CNFs films as flexible anode for high-performance lithium-ion batteries. Chem Eng J 369:215–222

39. Pan X, Duan X, Lin X, Lin XP, Zong FY (2018) Rapid synthesis of Cr-doped γ-Fe$_2$O$_3$/reduced graphene oxide nanocomposites as high performance anode materials for lithium ion batteries. J Alloys Compd 732:270–279

40. Wang J, Lin L, He D, Huang ZZ, Wang L, Song YH (2018) Self-assembly of Fe$_2$O$_3$ nanotubes on graphene as an anode material for lithium ion batteries. J Alloys Compd 750:871–877

41. Leela RA, Srivastava A, Gowda SR, Gullapalli H, Ajayan PM (2010) Synthesis of nitrogen-doped graphene films for lithium battery application. ACS Nano 4(11):6337–6342

42. Chen XF, Zhu XY, Cao GP, Zhang ST, Mu Y, Ming H, Qiu JY (2021) Fe$_3$O$_4$-based anodes with high conductivity and fast ion diffusivity designed for high-energy lithium-ion batteries. Energy Fuels 35:1810–1819

43. Li Q, Wang H, Ma J, Yang X, Yuan R, Chai YQ (2018) Porous Fe$_2$O$_3$-C microcubes as anodes for lithium-ion batteries by rational introduction of Ag nanoparticles. J Alloys Compd 735:840–846

44. Li Z, Li L, Zhong W, Cheng A, Fu WH, Li ZH, Zhang HY (2018) Simple and efficient fabrication of pomegranate-like Fe₂O₃@C on carbon cloth as an anode for lithium-ion batteries. J Alloys Compd 766:253–260

45. Sun Y-H, Liu S, Zhou F-C, Nan JM (2016) Electrochemical performance and structure evolution of core-shell nano-ring α-Fe₂O₃@Carbon anodes for lithium-ion batteries. Appl Surf Sci 390:175–184

46. Yang Z, Su D, Yang J, Wang J (2017) Fe₃O₄/C composite with hollow spheres in porous 3D-nanostructure as anode material for the lithium-ion batteries. J Power Sources 363:161–167

47. Zheng Z, Li P, Huang J, Zao Y, Zhang L (2020) High performance columnar-like Fe₂O₃@carbon composite anode via yolk@shell structural design. J Energ Chem 41:126–134

48. Sheng LC, Xi Y, Yu ZB, Qian ZX, Jun X, Chi XQ, Li JF (2020) 2D Mesoporous nanomesh from N-doped carbon-encapsulated V₂O₃ nanowires as an anode for lithium-ion batteries. J Phys Chem C 124(44):24073–24080

49. Li YW, Huang Y, Zheng YY, Huang RS, Yao JH (2019) Facile and efficient synthesis of α-Fe₂O₃ nanocrystals by glucose-assisted thermal decomposition method and its application in lithium ion batteries. J Power Sources 416:62–71

Publisher's Note Springer Nature remains neutral with regard to jurisdictional claims in published maps and institutional affiliations.